

# Guided anisotropic oxygen transport in vacancy ordered oxides

Zhenzhong Yang (✉ [zzyang@phy.ecnu.edu.cn](mailto:zzyang@phy.ecnu.edu.cn))

Pacific Northwest National Laboratory

**Le Wang**

Pacific Northwest National Laboratory <https://orcid.org/0000-0002-7730-9482>

**Mark Bowden**

Pacific Northwest National Laboratory

**Wen Liu**

Pacific Northwest National Laboratory

**Zihua Zhu**

Pacific Northwest National Laboratory <https://orcid.org/0000-0001-5770-8462>

**Chongmin Wang**

Pacific Northwest National Laboratory <https://orcid.org/0000-0003-3327-0958>

**Scott Chambers**

Pacific Northwest National Laboratory <https://orcid.org/0000-0002-5415-043X>

**Peter Sushko**

Pacific Northwest National Laboratory <https://orcid.org/0000-0001-7338-4146>

**Yingge Du**

Pacific Northwest National Laboratory <https://orcid.org/0000-0001-9680-1950>

---

## Article

**Keywords:** In situ TEM, phase transition, metastable intermediate phase, oxygen diffusion, oxygen vacancy channel, Brownmillerite

**Posted Date:** May 23rd, 2022

**DOI:** <https://doi.org/10.21203/rs.3.rs-1667305/v1>

**License:**  This work is licensed under a Creative Commons Attribution 4.0 International License.

[Read Full License](#)

---

**Version of Record:** A version of this preprint was published at Nature Communications on September 28th, 2023. See the published version at <https://doi.org/10.1038/s41467-023-40746-4>.

# Abstract

Anisotropic and efficient transport of ions under external stimuli governs the operation and failure mechanisms of energy-conversion systems and microelectronics devices. However, fundamental understanding of ion hopping processes is impeded by the lack of atomically precise materials and probes that allow for the monitoring and control at the appropriate time- and length- scales. In this work, using in situ transmission electron microscopy, we directly show that oxygen ion migration in vacancy ordered, semiconducting SrFeO<sub>2.5</sub> epitaxial thin films can be guided to proceed through two distinctly different diffusion pathways, each resulting in different polymorphs of SrFeO<sub>2.75</sub> with different ground electronic properties before reaching a fully oxidized, metallic SrFeO<sub>3</sub> phase. The diffusion steps and reaction intermediates are revealed by means of ab initio calculations. The principles of controlling oxygen diffusion pathways and reaction intermediates demonstrated here can significantly advance the rational design of structurally ordered oxides for tailored applications.

## Full Text

ABO<sub>3</sub>-type perovskite-structured transition metal oxides and their structural variances (e.g., Ruddlesden-Popper, Brownmillerite, infinite-layer phases) have been extensively studied because of their remarkable physico-chemical properties, including metal-to-insulator transition (MIT)<sup>1-4</sup>, superconductivity<sup>5,6</sup>, ferroelectricity<sup>7,8</sup>, notably high ionic conduction<sup>9,10</sup>, and surface catalytic activity<sup>11-14</sup>. Oxygen-based defects, which may be present as isolated oxygen vacancies (V<sub>O</sub>), vacancy clusters, or ordered oxygen vacancy channels (OVCs), can affect and even dominate these properties<sup>4,15-19</sup>. The topotactic phase transitions (TPT) as a result of oxygen content change can lead to intriguing concurrent changes in electronic, optical, and magnetic properties<sup>16,18,19</sup>. Memristors, synaptic transistors, and high-density memories based on such TPTs have been designed and tested, offering significant promise in the future oxide electronics and neuromorphic computing<sup>4,20,21</sup>. Reliability of the existing types of devices and our ability to create novel and robust signal processing systems are predicated on the understanding of the coupling between composition, structure, electronic properties, and external stimuli.

Strontium ferrite (SrFeO<sub>x</sub>) is a convenient platform to study reversible redox activity and associated property changes. Oxygen-deficient brownmillerite-structured SrFeO<sub>2.5</sub> (*BM-SFO*) (**Fig. 1a** and **Fig. 1c**), with ordered oxygen vacancy channels, can exhibit facile, highly anisotropic oxygen ion transport and low energy diffusion barriers within the OVCs, making these materials attractive for use as electrocatalysts and oxygen membranes<sup>16,17</sup>. *BM-SFO* is a G-type antiferromagnetic insulator, whereas the stoichiometric perovskite-structured SrFeO<sub>3</sub> (*P-SFO*) (**Fig. 1b**) is an antiferromagnetic metal<sup>4,15</sup>, which suggests that a zoo of transitory electronic behaviors may be realized by accessing metastable phases along the *BM-SFO* → *P-SFO* transition pathways. For example, memristive switching behavior is attributed to the dynamic formation/breaking of a conductive *P-SFO* filament in the parent matrix of insulating *BM-SFO*<sup>22,23</sup>. However, an atomistic understanding that bridges the evolution of the microstructure and properties in such materials is still lacking, preventing their predictive and practical use.

In this work, we show that controlling the orientation of the OVCs by epitaxial growth allows us to exploit the structural anisotropy to stabilize isomeric yet structurally and electronically distinct intermediates ( $\text{SrFeO}_{2.75}$ ). We use *in situ* transmission electron microscopy (TEM) to directly activate and image the TPT from *BM*-SFO to *P*-SFO, where oxygen ions are supplied from the reducible substrates under a built-up electric field created by electron beam irradiation during TEM imaging. Oxygen diffusion pathways that allow us to selectively access metastable reaction intermediate phases are revealed using density functional theory (DFT) calculations. Our results provide atomic scale insights into oxygen diffusion and redox-driven phase transition processes occurring in vacancy ordered oxides, paving the way for a deliberate control of the metastable phases.

### Oxidation of *BM*-SFO by *in situ* TEM

**Figure 1a** and **1c** show the structure model (viewed along [010]) of *BM*-SFO with two orientations of OVCs. *BM*-SFO is composed of alternating oxygen-deficient  $\text{FeO}_4$  tetrahedral layers (i.e., OVCs) and fully coordinated  $\text{FeO}_6$  octahedral layers. If OVCs are aligned parallel to the interface (**Fig. 1a**), oxygen ion ( $\text{O}^{2-}$ ) diffusion along the out-of-plane direction (i.e., from octahedral  $\text{FeO}_6$  sublayers to tetrahedral  $\text{FeO}_4$  sublayers) would proceed with a higher energy barrier<sup>21,24</sup>. In contrast, if OVCs are perpendicular to the interface (**Fig. 1c** and **Fig. 1d**),  $\text{O}^{2-}$  migrating from the substrate can directly intercalate into OVCs without crossing the  $\text{FeO}_6$  layers and, therefore, with a lower energy barrier. We design and grow epitaxial *BM*-SFO thin films with controlled orientations to reveal how OVC ordering can affect oxygen diffusion. By tuning the growth parameters and lattice mismatch between *BM*-SFO and substrates, we were able to stabilize OVCs to be either parallel to the interface with  $\text{SrTiO}_3$  (STO) (**Fig. 1e**) or perpendicular to the interface with  $(\text{LaAlO}_3)_{0.3}(\text{Sr}_2\text{AlTaO}_6)_{0.7}$  (LSAT) (**Fig. 1f**). The periodic contrast shown in the high-angle annular dark-field scanning TEM (HAADF-STEM) images (**Fig. 1e** and **Fig. 1f**) are characteristic of vacancy ordering in *BM*-SFO, where the OVCs appear as dark stripes repeating in alternate layer<sup>15,19,25</sup>. The controlled orientation of OVCs is also revealed by XRD  $\theta - 2\theta$  scans along the out-of-plane direction (**Supplementary Fig. S1**).

*In situ* TEM is used to drive the oxidation of *BM*-SFO and monitor subsequent phase transitions. It has been shown that electron beam illumination on an insulating sample during TEM imaging can generate secondary and Auger electrons that subsequently leave the sample surface<sup>26-29</sup>. The outer shell of the sample can become positively charged due to the loss of these electrons and an additional electric field is generated (**Fig. 1g** and **Supplementary Fig. S2**). It has been reported that a few volts can be induced at an electron beam dose of  $10^3$ - $10^4$   $\text{e}/(\text{\AA}^2 \text{ s})$ <sup>30</sup>, which could be sufficient to drive the O ions migration from the reducible substrate STO or LSAT to *BM*-SFO<sup>15,31</sup>. Furthermore, the samples are heated to elevated temperatures (200 to 300 °C) in our setup during *in situ* TEM experiments, allowing us to further tune the reaction speed so that the structural evolution from *BM*-SFO to *P*-SFO can be monitored at an appropriate time scale.

### Oxygen ion diffusion across the OVC layers

*In situ* TEM studies on *BM*-SFO/STO, in which OVCs are parallel to the interface (**Fig. 1a** and **1e**), allowed us to capture the dynamical phase transition processes (**Supplementary Movie S1**, recorded under 300 °C sample heating). Figures **2a-2c** show snapshot TEM images taken from **Movie S1**, demonstrating the formation and evolution of the *P*-SFO phase in the *BM*-SFO matrix. It took almost 4 minutes for the nucleation of *P*-SFO phase, due to the simultaneous O loss in SFO that happens at the relatively high-temperature heating of 300 °C under vacuum. High-resolution TEM images corresponding to the starting *BM*-SFO and emerging *P*-SFO are shown in the top panels of **Fig. 2d** and **2f**, respectively. As shown in the bottom panels of **Fig. 2d** and **2f**, the Fast Fourier Transform (FFT) patterns (left) obtained from the TEM images match well with the simulated diffraction patterns (right) that were based on the crystal structures of the corresponding phases. Furthermore, HAADF and annular bright-field (ABF)-STEM imaging for *BM*-SFO and *P*-SFO phases are also conducted, shown in **Supplementary Fig. S3**, to demonstrate the details of structure change at atomic scale.

It is worth to note that the formed *P*-SFO phase can quickly transform back to *BM*-SFO if the electron beam is blanked as we conduct the *in situ* TEM experiment at elevated temperature (300 °C), suggesting rapid O emission from *P*-SFO due to vacuum annealing. We used a lower heating temperature of 200 °C during another *in situ* TEM experiment to slow down the O loss process, which also allowed us to capture an intermediate phase displaying a checkerboard-like structure in the transition regions (see **Supplementary Movie S2** and **Fig. 2e**). At this time, it took about 1 minute and a half for the starting of phase transition, which is much shorter than the waiting time for *P*-SFO nucleation under heating temperature of 300 °C, suggesting the much slower O emission from SFO thin film under 200 °C. The intermediate phase's FFT pattern well matches with the simulated diffraction pattern of a previously observed SrFeO<sub>2.75</sub> phase (Cmmm space group)<sup>32</sup>. The structure of the SrFeO<sub>2.75</sub> phase (**Fig. 2e and 2g**) shows a checkerboard pattern composed of alternating columns of octahedral FeO<sub>6</sub> and pyramidal FeO<sub>5</sub>. This ordering corresponds to the formation of oxygen-deficient FeO<sub>5</sub> connectivity (chain of V<sub>O</sub>s) along the beam projection direction.

As the experiments were conducted in ultra-high vacuum, there is no other oxygen source but the STO substrates. In addition, according to the built-up electrical field shown in **Fig. 1g**, we expect the oxygen ions needed to heal the V<sub>O</sub>s to form SrFeO<sub>2.75</sub> or *P*-SFO should come from the reducible STO substrate, resulting in local oxygen deficiency at the vicinity of film/STO interface. To further confirm this, we collected cross-sectional STEM-electron energy loss spectroscopy (EELS) maps at the SFO/STO heterostructure at room temperature after *in situ* TEM experiments. As shown in **Supplementary Fig. S4**, the O intensity for STO exhibits a visible decrease in the region close to the SFO/STO interface (~ 30 nm in width), supporting our hypothesis. The emergence of clusters-like contrast (indicated by circles in **Supplementary Fig. S4**) close to the SFO/STO interface also indicates the agglomeration of V<sub>O</sub>s<sup>33,34</sup>.

To further visualize the oxygen exchange between SFO and STO, we performed <sup>18</sup>O labeled, time-of-flight secondary-ion mass spectrometry (ToF-SIMS) analysis. One *BM*-SFO/STO sample (~ 15nm thickness) was first annealed in vacuum at 700 °C for 30 min to promote oxygen loss in SFO, which would

subsequently draw oxygen from the STO substrate. After vacuum annealing, the SFO/STO sample, together with an untreated STO(001) substrate (reference STO thereafter), were annealed at 650°C for 0.5 h in a tube furnace backfilled with 50 Torr of  $^{18}\text{O}_2$ . The depth profiles of the  $^{18}\text{O}$  enrichment level ( $c$ , defined as  $^{18}\text{O}/(^{18}\text{O}+^{16}\text{O})\times 100$ ) for both samples are shown in **Fig. 2h**. Enhanced  $^{18}\text{O}$  enrichment (47%) is observed at the near-surface region of reference STO, which undergoes an exponential decay to natural abundance level ( $\sim 0.2\%$ ) within a  $\sim 40$  nm range. In comparison, the  $^{18}\text{O}$  enrichment level is significantly higher ( $\sim 80\%$  in SFO film) in the *BM*-SFO/STO sample. Importantly,  $c$  is found to be even higher (up to 87%) on the STO side close to the interface. The hump observed in **Fig. 2h** clearly reveals that there was an oxygen deficiency in STO which has been replenished by  $^{18}\text{O}_2$  annealing. Both STEM-EELS and ToF-SIMS data support that oxygen ions can migrate from STO to SFO film side.

To reveal the electronic and structural changes upon *BM*-SFO oxidation and the details of the oxygen diffusion pathways, we turn to DFT simulations (details are summarized in **Methods**). We mimic the experimentally observed O transfer from STO to  $\text{SrFeO}_x$  by continuously incorporating O atoms into one OVC plane of the *BM*-SFO supercell. Our calculations show that such O accumulation is thermodynamically preferred up to  $x \sim 2.7$  (**Fig. 4a**). These additional O species pull electron charge from the neighboring ions and, as formally  $\text{O}^{2-}$  ions ( $2p^6$ ), diffuse along the OVC parallel to the interface with STO with the calculated barrier of  $\sim 0.65$  eV (**Supplementary Fig. S5**). Further incorporation of O into the same OVC until all vacant sites are occupied ( $x = 2.75$  for the supercell used here) is cost neutral. This configuration corresponds to the formation of a full *P*-SFO layer, accordingly, the *P*-SFO/*BM*-SFO interface advances to the next OVC layer. We define the  $\text{SrFeO}_{2.75}$  intermediate formed through vacancy layer accumulation as *LA*-SFO as shown in **Fig. 4a**. As the concentration of the additional O species in the OVC increases, the number of vacant sites available for their diffusion decreases which slows the in-plane diffusion down. At the same time, O species in the vicinity of the *P*-SFO/*BM*-SFO interface become progressively less negative due to a competition between the preferred  $\text{O}^{2-}$  and  $\text{Fe}^{3+}$  electronic configurations, which leads to the formation of  $\text{O}^{(2-\delta)-}$  ( $2p^{6-\delta}$ ) and  $\text{Fe}^{3+\gamma}$  ( $3d^{5-\gamma}$ ) ions (see **Supplementary Fig. S6**). This depletion of the O  $2p$  band destabilizes the oxygen sublattice, thus promoting local restructuring. We found that for the fixed concentration of additional oxygens ( $x = 2.75$ ), distributing them over all OVCs, rather than confining them to one OVC is energetically preferred (**Fig. 4a**). The most stable configuration corresponds to the bulk  $\text{SrFeO}_{2.75}$  phase (purple dot in **Fig. 4a**), as observed experimentally (**Fig. 2e**) and illustrated in **Fig. 2g**.

To shed light on the kinetics of the lattice reorganization, we investigated the mechanisms of oxygen ion diffusion across the  $\text{FeO}_6$  layer into the next OVC in the out-of-plane direction, as schematically indicated in **Fig. 1a**. Our simulations suggest that this diffusion proceeds via a two-step mechanism (A–B–C path in **Fig. 4b**), whereby each step has the barrier of  $\sim 0.6$  eV. Notably, the transient configuration (B) formed after the first diffusion step can reverse to the original configuration (A) with the barrier of only 0.1 eV, which renders the overall diffusion barrier across the  $\text{FeO}_6$  plane of  $\sim 1.1$  eV, i.e., nearly twice as large as that for diffusion within an OVC plane ( $\sim 0.65$  eV). Since the formation of bulk-SFO $_{2.75}$  requires a

diffusion process disrupting continuous  $\text{FeO}_6$  planes by forming checkerboard arrangements of  $\text{FeO}_6$  and  $\text{FeO}_5$  polyhedra, we refer to it as disruptive diffusion (*DD*) thereafter and the corresponding bulk phase as *DD-SFO*<sub>2.75</sub> (**Fig. 4a**).

### Oxygen ion diffusion within the OVCs

We now consider the case of *BM-SFO/LSAT*, in which OVCs are perpendicular to the interface (**Fig. 1c** and **1f**). As shown in **Supplementary Movies S3-4**, compared to *BM-SFO/STO*, the phase transition occurred more readily (almost no waiting time) in *BM-SFO/LSAT* during *in situ* electron beam shower and 200°C sample heating. And this is because of the low diffusion barrier and high migration rate of O ions along OVCs in *BM-SFO*. Interestingly, two reaction fronts can be observed during the phase transition process, indicating a two-step reaction during the oxidation from *BM-SFO* to *P-SFO*. In **Fig. 3a-d**, the sequences of TEM images taken from **Movie S3** clearly show the phase transformation from *BM-SFO* (**Fig. 3a** and **3e**) to *P-SFO* (**Fig. 3d** and **3g**). **Figure 3b** and **3c** capture an intermediate phase separated by two reaction fronts (marked by white and yellow dashed lines). A magnified view of the intermediate phase circled in **Fig. 3b** is displayed in **Fig. 3f**. High-resolution HAADF-STEM image (**Fig. 3h**) together with its lattice spacing mapping (**Fig. 3i**) clearly reveal the phase boundaries, and the three phases are assigned as *BM-SFO*, *SrFeO*<sub>2.75</sub>, and *P-SFO*. The experimentally measured Sr-Sr in-plane spacings for *BM-SFO* are ~ 4.3 Å and 3.4 Å, due to the modulations from  $\text{FeO}_4$  and  $\text{FeO}_6$  connectivity, respectively (**Fig. 3j**). In contrast, the Sr-Sr distance of *P-SFO* is converged to one value of around 3.9 Å (**Fig. 3j**), as expected from a cubic structure coherently strained to an LSAT substrate. Compared to *BM-SFO* (*SrFeO*<sub>2.5</sub>), the Sr-Sr atomic distances of the intermediate phase are measured to be ~ 4.0 Å and 3.8 Å, respectively (**Fig. 3j**). According to our DFT modeling, the intermediate phase has a stoichiometry of *SrFeO*<sub>2.75</sub>, but its structure is significantly different from the bulk-*SFO*<sub>2.75</sub> phase shown in **Fig. 2g**. In this case, oxygen ion migration from the reducible LSAT substrate could directly intercalate into the OVCs without involving mass transfer from/to the  $\text{FeO}_6$  sublayers. The *SrFeO*<sub>2.75</sub> structure contains OVCs characteristic of  $\text{FeO}_5$  pyramidal connectivity (model in **Fig. 3f**) as a result of selectively healing  $V_{\text{O}_s}$ . The decrease in the IP Sr-Sr atomic distance between the sub-stoichiometric layers compared to *BM-SFO* is expected due to partial healing of  $V_{\text{O}_s}$ <sup>19,35,36</sup>.

To analyze the effect of oxygen incorporation and to establish the atomic structure of this intermediate phase, we examined stability of SFO depending on the arrangements of the oxygen species using DFT simulations. **Figure 1d** shows the side view (along [100] direction) of a vertically aligned OVC in which only connectivity of  $\text{FeO}_4$  tetrahedra is visible. Healing of the in-plane  $V_{\text{O}}$  indicated by solid red circles (defined as  $V_{\text{O-IP}}$ ) will lead to the formation of Fe-O-Fe bonds parallel to the interface. In comparison, the  $V_{\text{O}_s}$  formed between two Fe atoms along out-of-plane direction (indicated by dotted circles) are defined as  $V_{\text{O-ooP}}$ , and healing those will lead to Fe-O-Fe bonds perpendicular to the interface. Along the one-dimensional (1D)  $\text{FeO}_4$  tetrahedral chain, the energies needed to heal the alternating  $V_{\text{O-IP}}$  and  $V_{\text{O-ooP}}$  may vary depending on the sequence of oxygen incorporation and the substrate-induced strain. We

considered several configurations of the O species occupying  $V_{O-ip}$  only or  $V_{O-ooip}$  only sites and varied the concentration of these additional species (see **Fig. 4c**). According to our simulations for the 8·2·4 supercell (see **Methods**) at low O concentration, it is energetically favorable for the O to occupy  $V_{O-ooip}$  sites (blue symbols in **Fig. 4c**). The preference to occupy  $V_{O-ooip}$  over  $V_{O-ip}$  sites persists through the entire  $2.5 < x \leq 2.75$  range. An additional oxygen in the *BM*-SFO lattice is more stable at the  $V_{O-ooip}$  site than at the  $V_{O-ip}$  site by  $\sim 0.2$  eV. However, for the  $SrFeO_{2.75}$  phase, this energy difference reaches 0.35 eV (for Hubbard  $U = 0$  eV). Preferential occupation of the  $V_{O-ooip}$  sites is attributed to unconstrained lattice relaxation in the off-plane direction, while in-plane relaxation is suppressed due to epitaxial constraints. Accordingly, the out-of-plane lattice parameter decreases with increasing occupancy of the  $V_{O-ooip}$  sites and remains essentially unchanged with occupancy of the  $V_{O-ip}$  sites. At  $x = 2.75$ , our DFT modeling predicts that the stable structure should have all  $V_{O-ooip}$  sites occupied and all  $V_{O-ip}$  sites vacant (see **Supplementary Fig. S7**), which is selected as the structural model for the experimentally observed reaction intermediate shown in **Fig. 3f**. Moreover, Sr-Sr atomic distances (indicated by the dashed lines in **Fig. 3j**) of the modeled  $SrFeO_{2.75}$  are calculated to be  $\sim 4.0$  Å and  $3.7$  Å, respectively, which are in good agreement with the experimentally measured values. Since this  $SrFeO_{2.75}$  intermediate phase is derived by intercalation diffusion (*ID*) along the chains of adjacent  $V_{O-ip}$  or  $V_{O-ooip}$  sites (see **Fig. 1d**), we define it as *ID*-SFO<sub>2.75</sub> phase.

To obtain atomic-level insights into the kinetics of the oxidation process for the case of *BM*-SFO/LSAT, we determined the oxygen diffusion pathways and activation energies using DFT and a slab model, in which the *BM*-SFO film was explicitly strained to the substrate. Figure 4d shows the potential energy surface (PES) calculated by displacing an  $O^{2-}$  ion along the OVC and optimizing the positions of all other atoms at every step. The deep and shallow energy minima correspond to the  $O^{2-}$  occupying  $V_{O-ooip}$  and  $V_{O-ip}$  sites, respectively. The insets show the corresponding configurations of the selected  $O^{2-}$  ion (shown in red) migrating from the in-plane to out-of-plane to in-plane configuration. The steep rise of the left side of the plot reflects the interaction of the extra oxygen in the OVC and the stoichiometric substrate. The calculated diffusion barriers vary between  $\sim 0.6$  and  $\sim 0.8$  eV, suggesting that  $O^{2-}$  diffusion proceeds through the entire film with a preference of occupying the  $V_{O-ooip}$  sites, which explains the mechanism of the formation of the transient *ID*-SFO<sub>2.75</sub> phase observed experimentally.

### The electronic properties of intermediate phases

The compositional and structural differences between the SFO phases are reflected in the differences of their electronic properties. Figure 4e shows the one-electron densities of states (DOS) calculated for the *BM*-SFO, *DD*-SFO<sub>2.75</sub> with in-plane ( $\parallel$ ) and out-of-plane ( $\perp$ )  $FeO_5$  pyramidal connectivity, *ID*-SFO<sub>2.75</sub> with occupied out-of-plane O sites, and *P*-SFO. In the case of *BM*-SFO ( $x = 2.5$ ), both  $\parallel$  and  $\perp$  OVC configurations show a band gap of over 1 eV and nearly identical band edge DOS profiles. The band gap is underestimated with respect to the experimental values of  $\sim 2.0$  eV<sup>37</sup>, as expected for PBEsol. For  $x = 2.75$ , intercalation type diffusion (*ID*-SFO<sub>2.75</sub>) results in the band gap closure, indicating a metallic

behavior. In contrast, bulk-phase  $DD\text{-SFO}_{2.75}$  formed by oxidizing in-plane OVC remain non-metallic regardless of the orientation of the remaining  $V_O$  channels. As the oxygen content increases to  $x = 3.0$ , the DOS magnitude near the Fermi level increases continuously indicating enhanced metallic conductivity. The band gap closure upon increasing oxygen content from  $x = 2.5$  to  $x = 3.0$  is driven by the appearance of unoccupied Fe  $3d$  states (shown with shaded areas in **Fig. 4e**), which are depleted by incorporation of O species into the OVCs. Thus, electronic properties of the  $\text{SrFeO}_x$  films, particularly the onset for insulator-to-metal transition, can be controlled not only by changing the oxygen content but also by controlling the oxidation pathways to access the appropriate precursor phases.

In summary, we demonstrated the ability to promote and guide the transfer of oxygen species from reducible substrates to oxidize differently oriented  $BM\text{-SFO}$  thin films and monitor the structural changes and phase transitions using *in situ* TEM. By combining precisely controlled synthesis of precursor SFO with *in situ* control of the electron-beam-induced electric field and sample heating, we were able to activate oxygen diffusion along selected pathways in  $BM\text{-SFO}$  that allows us to access two different reaction intermediates – *Disruptive Diffusion-SFO* $_{2.75}$  and *Intercalation Diffusion-SFO* $_{2.75}$  phases. For the case of OVCs parallel to the interface, O diffusion is found to involve both  $\text{FeO}_6$  octahedral and  $\text{FeO}_4$  tetrahedral sublayers, where the phase transition from  $BM\text{-SFO}$  to  $P\text{-SFO}$  proceeds through a  $DD\text{-SFO}_{2.75}$  intermediate state via a disruptive diffusion process. In contrast, intercalation-only O diffusion is realized in samples displaying OVCs perpendicular to the interface, which results in a meta-stable  $ID\text{-SFO}_{2.75}$  phase containing alternating  $\text{FeO}_6$  octahedral and  $\text{FeO}_5$  pyramidal sublayers. Our DFT calculations predict that differences in crystal field associated with these two  $\text{SrFeO}_{2.75}$  intermediates result in qualitatively different electronic structures. It can be envisioned that selectively activating intercalation type diffusion may lead to faster ion transport, lower power assumption, and metastable intermediate with unique properties that can be harnessed for energy and information storage applications.

## Methods

**Thin film preparation.** Epitaxial  $\text{SrFeO}_{2.5}$  thin films with the thickness of 15–30 nm were grown on (001)-oriented  $\text{SrTiO}_3$  and LSAT single crystal substrates by using PLD.<sup>19</sup> The laser pulse (248 nm) energy density was  $\sim 2 \text{ J}\cdot\text{cm}^{-2}$ , the repetition rate was 1 Hz. The substrates were heated to 700 °C during deposition and the growth oxygen pressure was kept at 0.1 mTorr. After growth, the samples were cooled down to room temperature under the same oxygen pressure.

**In situ TEM experiments.** The TEM samples used for *in situ* TEM were prepared using a focus ion beam scanning electron microscopy (Helios). The cross-sectional lamella lifted out using FIB was thinned down to  $\sim 200$  nm at 30 kV, followed by 5kV and 2 kV milling down to  $\sim 50$  nm, and the 1 kV setting was used for the final milling. *In situ* TEM experiments were conducted using an FEI Titan 80–300 TEM equipped with an aberration corrector for the objective lens and a Gatan furnace-based heating holder. The accelerate voltage of 300 kV and electron beam dose rate of  $\sim 10^3 \text{ e}/(\text{\AA}^2 \text{ s})$  were used in the *in situ* TEM experiments. The TEM samples were heated to elevated temperatures (200 to 300 °C) during the

experiments to promote the reaction, making it suitable for *in situ* TEM observation. It should be noted that heating to temperatures in excess of 300 °C led to faster oxygen loss, promoting the partial reduction of the newly formed *P*-SFO phase. The high angle annular dark field (HAADF) scanning transmission electron microscopy (STEM) image, annular bright field (ABF) STEM image and electron energy loss spectrum (EELS) mapping were conducted using JEM ARM200F. The collection angle for HAADF and ABF imaging were 90–370 mrad and 10–23 mrad, respectively. The probe current of ~ 20 pA was used for STEM imaging and EELS mapping to minimize the electron beam induced phase transition. The Dual-EELS was used for the energy calibration of Fe-L edge with the simultaneously acquired zero loss spectrum.

**SIMS measurements.** ToF-SIMS measurements were performed using a ToF-SIMS V (ION-TOF GmbH, Münster, Germany) mass spectrometer equipped with a time-of-flight analyzer of a reflectron type. A dual-beam depth profiling strategy was used, in which a 1.0 keV Cs<sup>+</sup> beam (~40 nA, 200 μm × 200 μm scanning area) was used for sputtering and a 50 keV Bi<sub>3</sub><sup>2+</sup> beam (~0.05 pA, 50 μm × 50 μm scanning area at the Cs<sup>+</sup> crater center) was used for data collection. One *BM*-SFO sample was first annealed in vacuum at 700 °C for 0.5 h to promote further oxygen loss in SFO. After vacuum annealing, the SFO/STO sample, together with an untreated STO(001) substrate (Reference STO), were annealed at 650°C for 0.5 h in a tube furnace backfilled with 50 Torr of <sup>18</sup>O<sub>2</sub> (97% purity, Cambridge Isotopes). The SFO/STO interface location was confirmed by the secondary ion signals of Fe and Ti.

**Ab initio simulations.** Supported SrFeO<sub>x</sub> films were represented using two models. In the periodic slab model, the BO<sub>2</sub>-terminated substrate was represented by one unit cell of SrTiO<sub>3</sub> with the in-plane coordinates of all atoms fixed in their centro-symmetric positions. *BM*-SFO film supported on this substrate has the thickness equivalent to four crystallographic perovskite cells. The vacuum gap was set to ~ 15 Å. In the bulk model, the *BM*-SFO was represented by the supercell equivalent to the 4×4×4 cubic perovskite supercell. In both cases, we considered two orientations of the oxygen vacancy channels (OVCs) in *BM*-SFO – parallel and perpendicular to the substrate plane. In addition, we used 8×4×2 supercell for the OVCs perpendicular to the substrate to investigate the relative stability of configurations formed by partial occupancy of the in-plane and out-of-plane oxygen vacant sites. To investigate the strain effects, we considered four sets of in-plane lattice parameters ( $a = b$ ) corresponding to LaAlO<sub>3</sub> (3.790 Å), LSAT (3.868 Å), SrTiO<sub>3</sub> (3.905 Å), and DyTiO<sub>3</sub> (3.950 Å) substrates. In the bulk model, the off-plane lattice parameter was optimized.

The calculations were performed using the Vienna Ab initio Software Package (VASP)<sup>38,39</sup>. The Perdew-Burke-Ernzerhof exchange-correlation functional modified for solids (PBEsol)<sup>40</sup> and the projector augmented wave pseudopotentials<sup>41</sup>, as implemented in VASP, were used. The energy cut-off was 500 eV. Gamma point only was used for energy minimization with respect to the internal coordinates and the off-plane lattice parameter, the electronic structure for the energy minimum configuration was recalculated using 2×2×2 Monkhorst-Pack k-points mesh, 4×4×4 mesh for used for DOS calculations. The total energy was converged to 10<sup>-5</sup> eV. The Hubbard *U* correction for Fe 3*d* states ( $U_{eff} = U - J = 3$  eV)

was applied using Dudarev's approach<sup>42</sup>. The  $1 \times 2 \times 1$  k-mesh and ( $U_{eff} = 0$  eV) were used for the  $8 \times 2 \times 4$  supercell. Atomic charges were calculated using the Bader's approach<sup>43</sup>. The diffusion pathways and activation energies were calculated for the SrTiO<sub>3</sub> substrate ( $a = b = 3.905$  Å) using the nudged elastic band (NEB) method and eight NEB images unless stated otherwise. Energy gain due to oxygen incorporation was calculated with respect to the gas-phase O<sub>2</sub> molecule.

## Declarations

### Acknowledgments

This work was supported by the U.S. Department of Energy (DOE), Office of Science (SC), Office of Basic Energy Sciences (BES), Early Career Research Program under award # 68278. DFT simulations were supported by the DOE BES Division of Materials Sciences and Engineering under Award No. 10122. We thank Dr. Endong Jia for valuable discussions and help on the Figure layout. A portion of the research was performed using EMSL (Ringgold ID130367), a DOE User Facility sponsored by the Office of Biological and Environmental Research and located at the Pacific Northwest National Laboratory (PNNL). This research used resources of the National Energy Research Scientific Computing Center, a DOE SC User Facility supported by the SC of the DOE under Contract No. DE-AC02-05CH11231 using NERSC award BES-ERCAP0021800. PNNL is a multi-program national laboratory operated for DOE by Battelle under contract DE-AC05-76RL01830.

### Author contributions

Y.D. and Z.Y. designed and initiated the research. L.W. grew the thin film samples. Z.Y. conducted the *in situ* TEM experiments and performed data analysis. P.V.S. planned and performed the DFT calculations. M.B. performed XRD measurements. W.L. and Z.Z. performed the SIMS experiment. All authors participated in the discussion and interpretation of results. Z.Y., L.W., S.A.C., P.V.S. and Y.D. wrote the manuscript and all authors approved the final version.

### Competing interests

The authors declare no competing financial interests.

### Additional information

Supplementary information accompanies this paper can be found online.

## References

1. Khare A et al (2017) Topotactic Metal-Insulator Transition in Epitaxial SrFeO<sub>x</sub> Thin Films. Adv. Mater. **29**

2. Jeong J et al (2013) Suppression of metal-insulator transition in VO<sub>2</sub> by electric field-induced oxygen vacancy formation. *Science* 339:1402–1405
3. Jeon H et al (2013) Topotactic phase transformation of the brownmillerite SrCoO<sub>2.5</sub> to the perovskite SrCoO<sub>3.5</sub>. *Adv Mater* 25:3651–3656
4. Ge C et al (2019) A Ferrite Synaptic Transistor with Topotactic Transformation. *Adv Mater* 31:e1900379
5. Jorgensen JD et al (1988) Superconducting phase of La<sub>2</sub>CuO<sub>4-y</sub>: Superconducting composition resulting from phase separation. *Phys Rev B* 38:11337–11345
6. Li D et al (2019) Superconductivity in an infinite-layer nickelate. *Nature* 572:624–627
7. Becher C et al (2015) Strain-induced coupling of electrical polarization and structural defects in SrMnO<sub>3</sub> films. *Nat Nanotechnol* 10:661–665
8. Mishra R et al (2014) Oxygen-vacancy-induced polar behavior in (LaFeO<sub>3</sub>)<sub>2</sub>/(SrFeO<sub>3</sub>) superlattices. *Nano Lett* 14:2694–2701
9. Kim YM et al (2012) Probing oxygen vacancy concentration and homogeneity in solid-oxide fuel-cell cathode materials on the subunit-cell level. *Nat Mater* 11:888–894
10. Inoue S et al (2010) Anisotropic oxygen diffusion at low temperature in perovskite-structure iron oxides. *Nat Chem* 2:213–217
11. Murray R, Bard A (1984) Marcel Dekker, New York. *J. Electroanal. Chem.* **13**, 191
12. Wang L et al (2016) Oxygen Vacancy Induced Room-Temperature Metal-Insulator Transition in Nickelate Films and Its Potential Application in Photovoltaics. *ACS Appl Mater Interfaces* 8:9769–9776
13. Pena MA, Fierro JL (2001) Chemical structures and performance of perovskite oxides. *Chem Rev* 101:1981–2017
14. Wang L et al (2018) Tuning Bifunctional Oxygen Electrocatalysts by Changing the A-Site Rare-Earth Element in Perovskite Nickelates. *Adv Funct Mater* 28:1803712
15. Zhang Q et al (2017) Atomic-resolution imaging of electrically induced oxygen vacancy migration and phase transformation in SrCoO<sub>2.5-δ</sub>. *Nat Commun* 8:104
16. Paulus W et al (2008) Lattice dynamics to trigger low temperature oxygen mobility in solid oxide ion conductors. *J Am Chem Soc* 130:16080–16085
17. Kendall K (1995) Recent developments in perovskite-based oxide ion conductors. *Solid State Ion* 82:215–223
18. Saleem MS et al (2019) Electric Field Control of Phase Transition and Tunable Resistive Switching in SrFeO<sub>2.5</sub>. *ACS Appl Mater Interfaces* 11:6581–6588
19. Wang L, Yang ZZ, Bowden ME, Du YG (2019) Brownmillerite phase formation and evolution in epitaxial strontium ferrite heterostructures. *Appl Phys Lett* 114:231602

20. Nallagatla VR et al (2020) Complementary Resistive Switching and Synaptic-Like Memory Behavior in an Epitaxial SrFeO<sub>2.5</sub> Thin Film through Oriented Oxygen-Vacancy Channels. *ACS Appl Mater Interfaces* 12:41740–41748
21. Nallagatla VR et al (2019) Topotactic Phase Transition Driving Memristive Behavior. *Adv Mater* 31:1903391
22. Tian J et al (2019) Nanoscale Topotactic Phase Transformation in SrFeO<sub>x</sub> Epitaxial Thin Films for High-Density Resistive Switching Memory. *Adv Mater* 31:e1903679
23. Acharya SK et al (2016) Epitaxial Brownmillerite Oxide Thin Films for Reliable Switching Memory. *ACS Appl Mater Interfaces* 8:7902–7911
24. Mitra C, Meyer T, Lee HN, Reboredo FA (2014) Oxygen diffusion pathways in brownmillerite SrCoO<sub>2.5</sub>: Influence of structure and chemical potential. *J Chem Phys* 141:084710
25. Khare A et al (2018) Directing Oxygen Vacancy Channels in SrFeO<sub>2.5</sub> Epitaxial Thin Films. *ACS Appl Mater Interfaces* 10:4831–4837
26. Jiang N (2016) Electron beam damage in oxides: a review. *Rep Prog Phys* 79:016501
27. Jiang N (2016) Beam damage by the induced electric field in transmission electron microscopy. *Micron* 83:79–92
28. Jiang N (2013) Damage mechanisms in electron microscopy of insulating materials. *J. Phys. D, Appl. phys.* **46**
29. Tao J et al (2017) Reversible structure manipulation by tuning carrier concentration in metastable Cu<sub>2</sub>S. *Proc. Natl. Acad. Sci.* **114**, 9832
30. Mildner S et al (2015) Environmental TEM Study of Electron Beam Induced Electrochemistry of Pr<sub>0.64</sub>Ca<sub>0.36</sub>MnO<sub>3</sub> Catalysts for Oxygen Evolution. *J Phys Chem C* 119:5301–5310
31. Jiang N (2012) On the oxidation of CaF<sub>2</sub> in transmission electron microscope. *Micron* 43:746–754
32. Hodges JP et al (2000) Evolution of Oxygen-Vacancy Ordered Crystal Structures in the Perovskite Series Sr<sub>n</sub>Fe<sub>n</sub>O<sub>3n-1</sub> (n = 2, 4, 8, and ∞), and the Relationship to Electronic and Magnetic Properties. *J Solid State Chem* 151:190–209
33. Muller DA, Nakagawa N, Ohtomo A, Grazul JL, Hwang H (2004) Y. Atomic-scale imaging of nanoengineered oxygen vacancy profiles in SrTiO<sub>3</sub>. *Nature* 430:657
34. Dudy L et al (2016) In Situ Control of Separate Electronic Phases on SrTiO<sub>3</sub> Surfaces by Oxygen Dosing. *Adv Mater* 28:7443–7449
35. Zhang KH et al (2014) Reversible nano-structuring of SrCrO<sub>3-δ</sub> through oxidation and reduction at low temperature. *Nat Commun* 5:4669
36. Lu N et al (2017) Electric-field control of tri-state phase transformation with a selective dual-ion switch. *Nature* 546:124–128
37. Nallagatla VR et al (2019) Topotactic Phase Transition Driving Memristive Behavior. *Adv Mater* 31:e1903391

38. Kresse G, Hafner J (1994) Ab initio molecular-dynamics simulation of the liquid-metal-amorphous-semiconductor transition in germanium. *Phys Rev B* 49:14251–14269
39. Kresse G, Furthmuller J (1996) Efficient iterative schemes for ab initio total-energy calculations using a plane-wave basis set. *Phys Rev B* 54:11169–11186
40. Perdew JP et al (2008) Restoring the density-gradient expansion for exchange in solids and surfaces. *Phys Rev Lett* 100:136406
41. Blochl PE (1994) Projector augmented-wave method. *Phys Rev B* 50:17953–17979
42. Dudarev SL, Botton GA, Savrasov SY, Humphreys CJ, Sutton AP (1998) Electron-energy-loss spectra and the structural stability of nickel oxide: An LSDA + U study. *Phys Rev B* 57:1505–1509
43. Tang W, Sanville E, Henkelman G (2009) A grid-based Bader analysis algorithm without lattice bias. *J Phys Condens Matter* 21:084204

## Figures

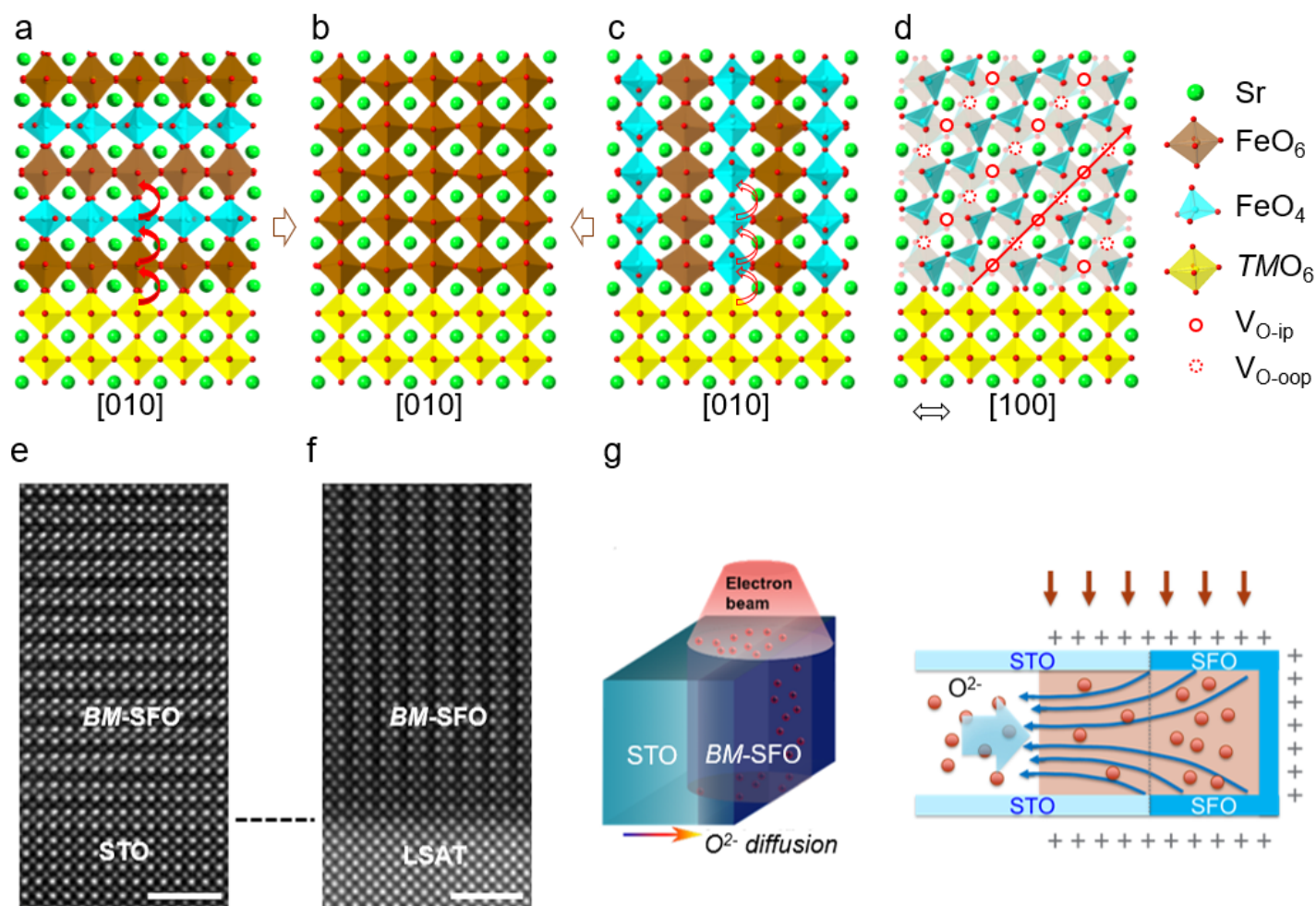
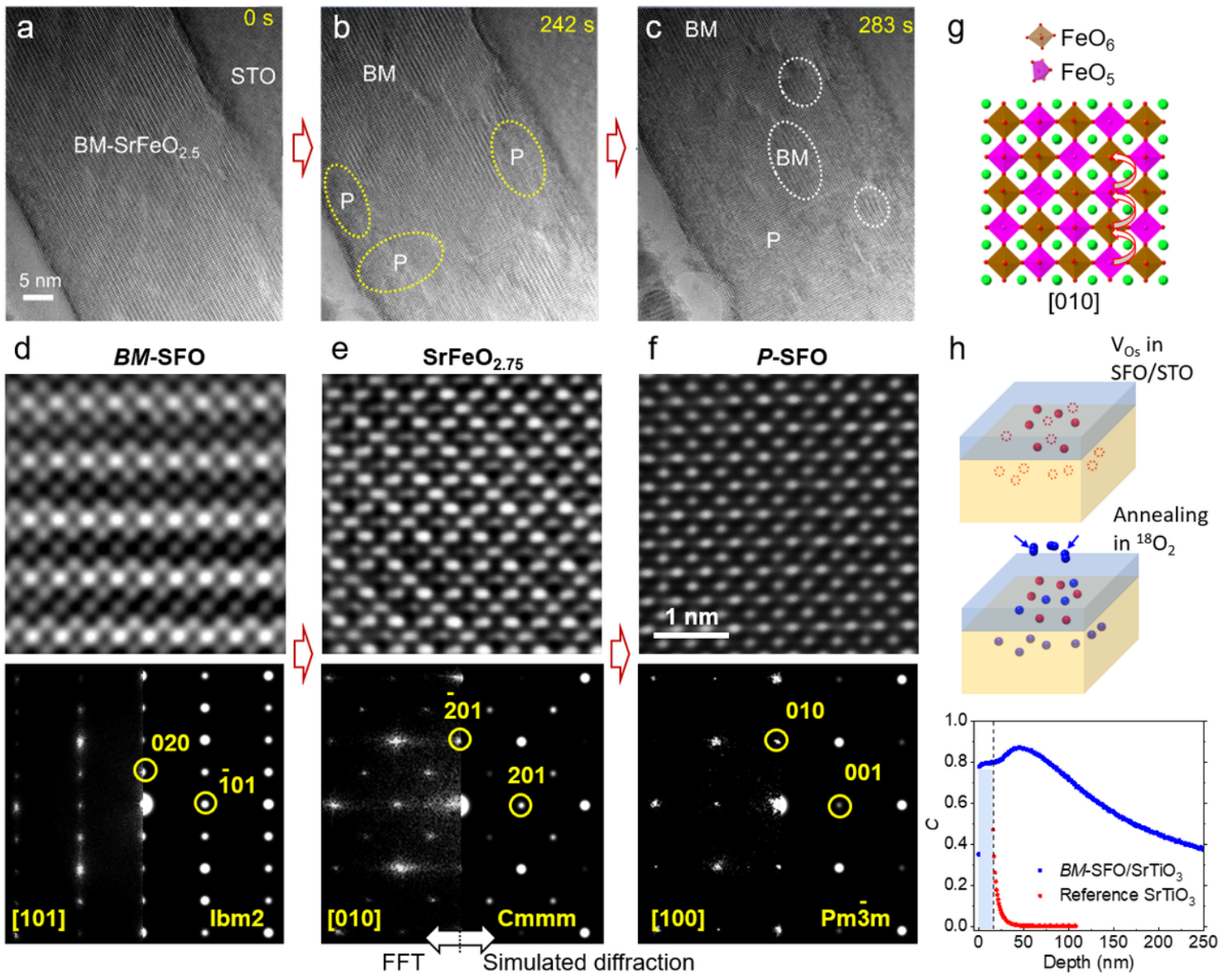


Figure 1

**Characterization of *BM*-SFO thin films and the concept of oxidation of *BM*-SFO by *in situ* TEM.** **a-c**, Structure models (projected along [010]) of (a) *BM*-SFO with OVCs // substrate, (b) *P*-SFO, and (c) *BM*-SFO with OVCs  $\perp$  substrate. **d**, Structure model highlighting an OVC plane shown in (c) but viewed along [100]. **e-f**, HAADF-STEM images of *BM*-SFO grown on STO(001) and LSAT(001), respectively, demonstrating the controlled orientation of OVCs. Scale bar is 2 nm. **g**, Schematic illustrations showing the electron-beam-induced electrical field (dark blue arrows) generated during TEM imaging and its effect in promoting  $O^{2-}$  diffusion. The red spheres represent  $O^{2-}$  ions moving in the opposite direction of electron-beam-induced electrical field.



**Figure 2**

**Phase transformations of *BM*-SFO  $\rightarrow$  SrFeO<sub>2.75</sub>  $\rightarrow$  *P*-SFO observed on *BM*-SFO/STO with starting OVCs // STO(001).** **a-c**, *In situ* TEM images taken from **Supplementary Movie S1** illustrating the phase transition process. **d-f**, High resolution TEM images (top), together with the Fast Fourier Transform patterns (bottom

left) and simulated diffraction patterns (bottom right) for (d) *BM-SFO*, (e)  $\text{SrFeO}_{2.75}$ , and (f) *P-SFO*. g, Structure model of bulk-like  $\text{SrFeO}_{2.75}$ . h, Schematics showing the creation of oxygen vacancies ( $V_{\text{O}_s}$ ) in SFO/STO by annealing in vacuum (top), and subsequent replenishment of oxygen by annealing in  $^{18}\text{O}_2$  (middle). ToF-SIMS depth profiles of  $^{18}\text{O}$  (bottom) display the enrichment level for a 15nm SFO film grown on STO(001) and a STO reference sample. The dashed line denotes the SFO/STO interface with SFO film on the left side.

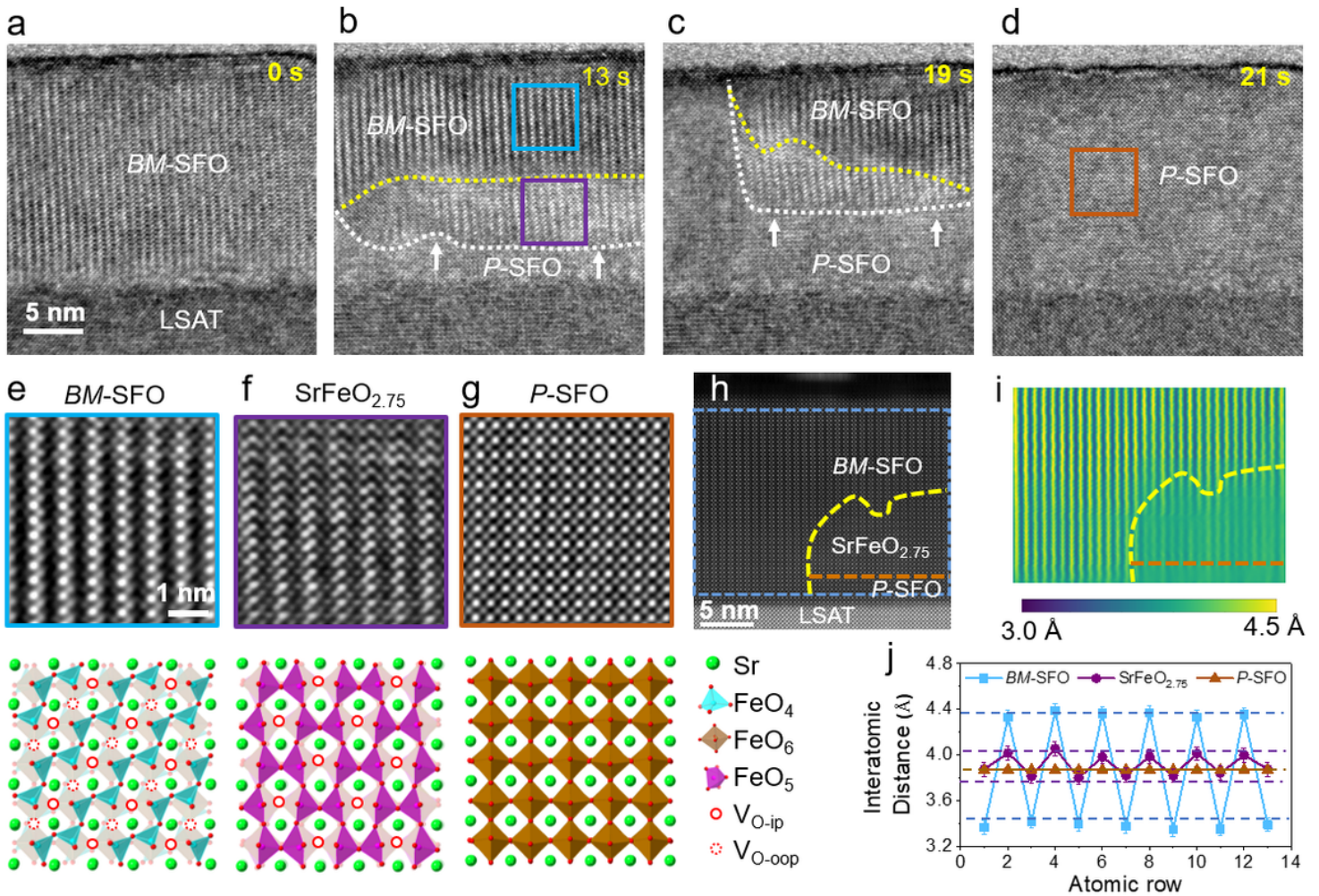


**Figure 3**

**Phase transformations of *BM-SFO*  $\rightarrow$   $\text{SrFeO}_{2.75}$   $\rightarrow$  *P-SFO* observed on *BM-SFO*/LSAT with starting OVCs  $\perp$  LSAT(001).** a-d, Time-stamped *in situ* TEM images taken from **Supplementary Movie S3** illustrating a two-step phase transition process. The yellow and white dashed lines indicate the two reaction fronts. e-g, High-resolution TEM images (top) matching the highlighted regions shown in (b) and (d) and their corresponding structure models (bottom). h, HAADF-STEM image of an SFO/LSAT sample showing the coexistence of three different phases. i, In-plane lattice spacing (between Sr-Sr ions) map of the blue box marked region shown in (h). j, Comparison of experimentally measured values (symbols) with DFT calculated results (dashed lines) for in-plane Sr-Sr interatomic distances among the three phases.

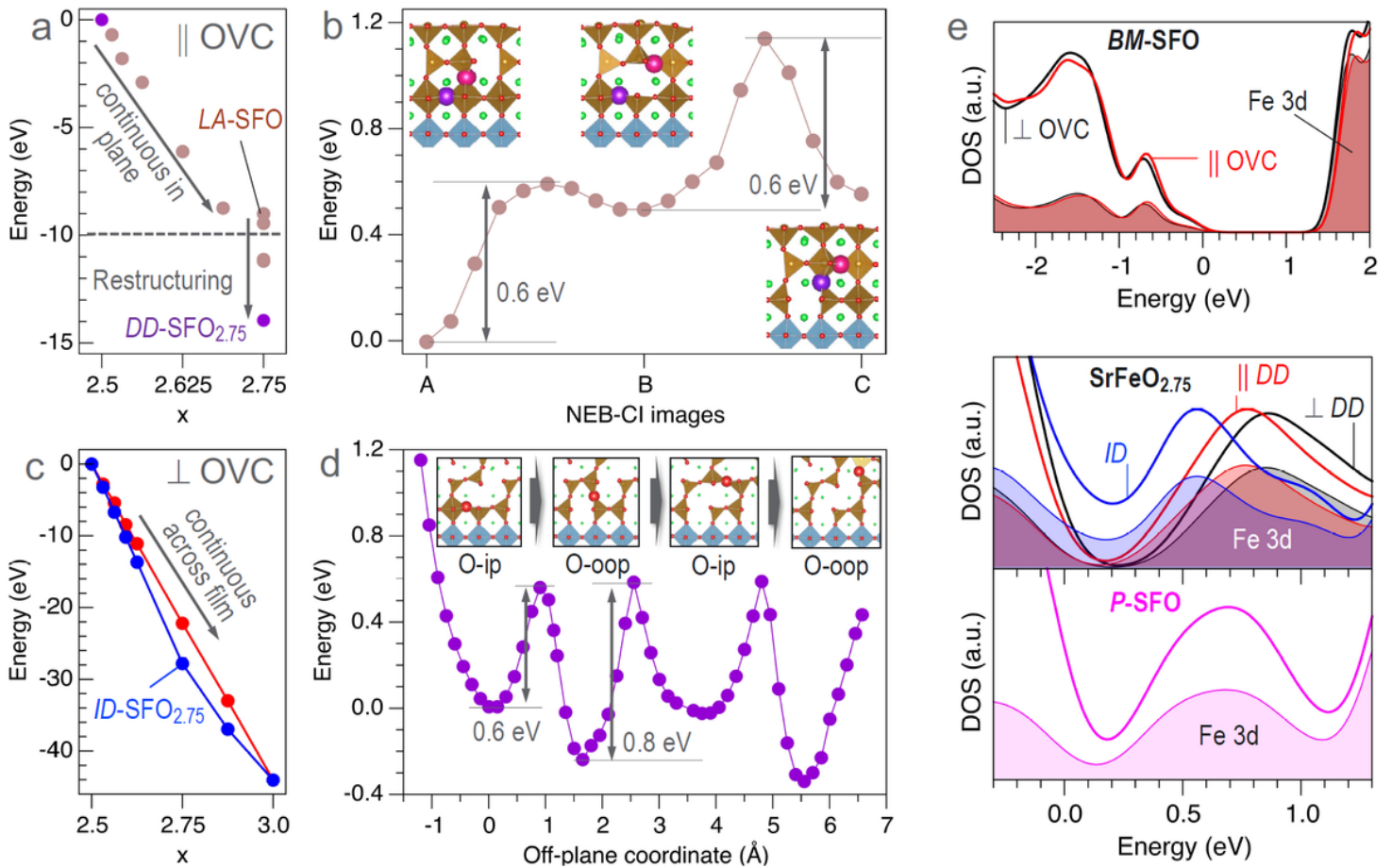


**Figure 4**

**DFT calculations of SFO stability, oxygen diffusion pathways, and electronic density of states.** **a**, Energy gain due to incorporation of oxygen into OVCs parallel ( $\parallel$ ) to the substrate. Incorporation proceeds continuously into one OVC layer up to  $\sim 75\%$  occupancy ( $x \sim 2.7$  in our supercell) with the formation of  $LA\text{-SFO}_{2.75}$  phase; reorganization of the oxygen sublattice at larger  $x$  through disruptive diffusion leads to the formation of  $DD\text{-SFO}_{2.75}$ . **b**, Potential energy surface (PES) for an  $\text{O}^{2-}$  (large spheres) diffusion across Fe-centered polyhedra (brown)  $\text{FeO}_6$  layers into a neighboring OVC calculated using nudged elastic band climbing image (NEB-Cl) method; insets show the initial and final configurations for each step; the transient configuration in between renders the overall diffusion barrier of  $\sim 1.1$  eV. **c**, Energy gain due to oxygen incorporation into OVCs perpendicular ( $\perp$ ) to the substrate ( $U_{\text{eff}}=0$  eV) for sequentially occupied  $V_{\text{O-ip}}$  and  $V_{\text{O-ooip}}$  sites (red) and sequentially occupied  $V_{\text{O-ooip}}$  and  $V_{\text{O-ip}}$  sites (blue), leading to the formation of the intercalation  $ID\text{-SFO}_{2.75}$  phase. **d**, PES for  $\text{O}^{2-}$  diffusion along  $\perp$ OVC. Insets show the local atomic configurations for the first four minima. **e**, One-electron density of states (DOS) for  $BM\text{-SFO}$  ( $x = 2.5$ ),  $ID$ - and  $DD\text{-SFO}_{2.75}$ , and  $P\text{-SFO}$  ( $x = 3$ ) phases. Shaded areas show DOS projected on Fe 3d states. Fermi energy is at 0 eV.

## Supplementary Files

This is a list of supplementary files associated with this preprint. Click to download.

- [SI.docx](#)
- [MovieS1.mp4](#)
- [MovieS2.mp4](#)
- [MovieS3.mp4](#)
- [MovieS4.mp4](#)